PNAS RESEARCH ARTICLE | CHEMISTRY

In situ turning defects of exfoliated Ti_3C_2 MXene into Fenton-like catalytic active sites

Yue Jiang (姜越)[a,b], Didar Baimanov[c,d], Shan Jin[e], Japhet Cheuk-Fung Law[f], Pengcheng Zhao[a,g], Juanjuan Tang[a,b], Jian Peng[a,b], Liming Wang[c], Kelvin Sze-Yin Leung[f], Wenchao Sheng[a,g], and Sijie Lin (林思劼)[a,b,1]

Edited by Alexis Bell, University of California, Berkeley, CA; received June 14, 2022; accepted November 8, 2022

Controllable in situ formation of nanoclusters with discrete active sites is highly desirable in heterogeneous catalysis. Herein, a titanium oxide–based Fenton-like catalyst is constructed using exfoliated Ti_3C_2 MXene as a template. Theoretical calculations reveal that a redox reaction between the surface Ti-deficit vacancies of the exfoliated Ti_3C_2 MXene and H_2O_2 molecules facilitates the in situ conversion of surface defects into titanium oxide nanoclusters anchoring on amorphous carbon (TiO_x@C). The presence of mixed-valence $Ti^{\delta+}$ (δ = 0, 2, 3, and 4) within TiO_x@C is confirmed by X-ray photoelectron spectroscopy (XPS) and X-ray absorption fine structure (XAFS) characterizations. The abundant surface defects within TiO_x@C effectively promote the generation of reactive oxygen species (ROS) leading to superior and stable Fenton-like catalytic degradation of atrazine, a typical agricultural herbicide. Such an in situ construction of Fenton-like catalysts through defect engineering also applies to other MXene family materials, such as V_2C and Nb_2C.

heterogeneous catalysis | in situ | MXene | multivalence | template synthesis

Significance

Anchoring nanoscale active sites on a substrate has proven to be an effective way to maximize catalytic performance. Herein, we report a strategy to turn surface defects into Fenton-like catalytic active sites in situ. The Ti-deficit vacancies of the exfoliated Ti_3C_2MXene were transformed to discrete titanium oxide with multivalent Ti. The combined use of theoretical calculation and experimental characterizations revealed the superior and stable Fenton-like catalytic activity toward degradation of a typical herbicide, atrazine. Our results showcased an elegant and a universal use of MXene family materials as templates and multivalent metal precursors for the in situ formation of Fenton-like catalysts.

Developing effective and reliable Fenton-like heterogeneous catalysts serves an essential role in addressing the ever-growing environmental pollution and water security challenges in both scientific and industrial fields (1, 2). Heterogeneous catalysts with decreasing physical sizes, such as nanodots, atomic clusters, and single-atom catalysts (SACs), are of great interest due to the abundance of catalytic reaction sites (3–6). However, ultrasmall sizes are prone to aggregation due to the exponential increase of surface energy, resulting in blockage of active sites, instability, and poor recyclability (7–9). In this regard, utilizing a substrate to anchor active sites and maximize the dispersion degree has proven to be a promising strategy (10–12). Carbon-based two-dimensional nanomaterials, including graphene (13), carbon nitride (14), and N, S-doped carbon frameworks (15), showed the ability to trap, spatially confine, or bond metal clusters to reduce aggregation. But most of the formation of catalytic active metal oxides requires the addition of metal precursors (16, 17). Hence, it is appealing to explore substrates that contain a metal ingredient to offer opportunities for the in situ formation of catalytic active sites.

MXenes, an exciting family of two-dimensional transition metal carbides, nitrides, or carbonitrides (18–20), have shown clear advantages in energy and environmental remediation fields. The layered structure of MXene provides an ideal substrate for anchoring catalytic active sites. Double transition metal MXene nanosheets ($Mo_2TiC_2T_x$) immobilizing single Pt atoms showed excellent catalytic performance for hydrogen evolution (21). Interestingly, the etching process to remove Al layers from the MAX phase material would occasionally strip away transition metal atoms leaving single vacancies or vacancy cluster defects that are highly oxophilic (22, 23). These defect sites are highly reactive to form oxide clusters through hydrolysis or abstraction of oxygen. As a result, the compositing transition metals of MXene, i.e., Ti, V, and Nb, could become the source materials for the in situ formation of transition metal oxides. These transition metal elements with multivalence are poised to facilitate the reaction with H_2O_2 for Fenton-like catalysis (24–27).

Here, we propose an in situ construction of Fenton-like catalysts by turning surface defects into catalytic active sites. Exfoliated Ti_3C_2 MXene was subjected to mild oxidation by H_2O_2 to create titanium oxide nanoclusters anchoring on a silk-like carbon substrate (TiO_x@C). Density functional theory (DFT) calculations revealed that the redox reaction occurred at the Ti-deficit defects of exfoliated Ti_3C_2 MXene. The multivalence of Ti and surface defects in TiO_x@C were fully characterized by X-ray photoelectron spectroscopy (XPS), X-ray absorption fine structure (XAFS), and positron annihilation life spectroscopy (PALS). The effectiveness and stability of the Fenton-like catalytic activity were assessed based on the degradation of atrazine, a typical agriculture herbicide. The universalness of the strategy was also tested on other MXene family materials, including V_2C and Nb_2C.

Author contributions: Y.J. and S.L. designed research; Y.J., D.B., S.J., J.C.-F.L., P.Z., J.T., J.P., L.W., K.S.-Y.L., and W.S. performed research; Y.J., D.B., S.J., J.C.-F.L., P.Z., J.T., J.P., L.W., K.S.-Y.L., W.S., and S.L. analyzed data; and Y.J. and S.L. wrote the paper.

The authors declare no competing interest.

This article is a PNAS Direct Submission.

[1]To whom correspondence may be addressed. Email: lin.sijie@tongji.edu.cn.

This article contains supporting information online at https://www.pnas.org/lookup/suppl/doi:10.1073/pnas.2210211120/-/DCSupplemental.

Published December 27, 2022.

Results and Discussion

In Situ Formation of Carbon-Supported Titanium Oxide (TiO_x@C) Templated by Exfoliated MXene. Fig. 1*A* illustrates the main steps of in situ formation of TiO_x@C. Bulk Ti_3AlC_2 with its Al layer etched away by hydrofluoric acid (HF) was further treated with H_2O_2. The typical accordion-like structure of Ti_3C_2 MXene under scanning electron microscopy (SEM) demonstrated a successful etching of the Al layer (Fig. 1 *B* and *C*). The final product displayed a silk-like structure in light gray color decorated with darker dots of 2 to 5 nm on a microscopic scale and a uniform and stably-dispersed yellow-orange suspension showing the Tyndall effect (Fig. 1 *D*, *Inset*). Elemental analysis (energy-dispersive X-ray spectroscopy mapping) confirmed the absence of the Al element in the etched Ti_3C_2 MXene (*SI Appendix*, Fig. S1). electron paramagnetic resonance (EPR) analysis showed a clear

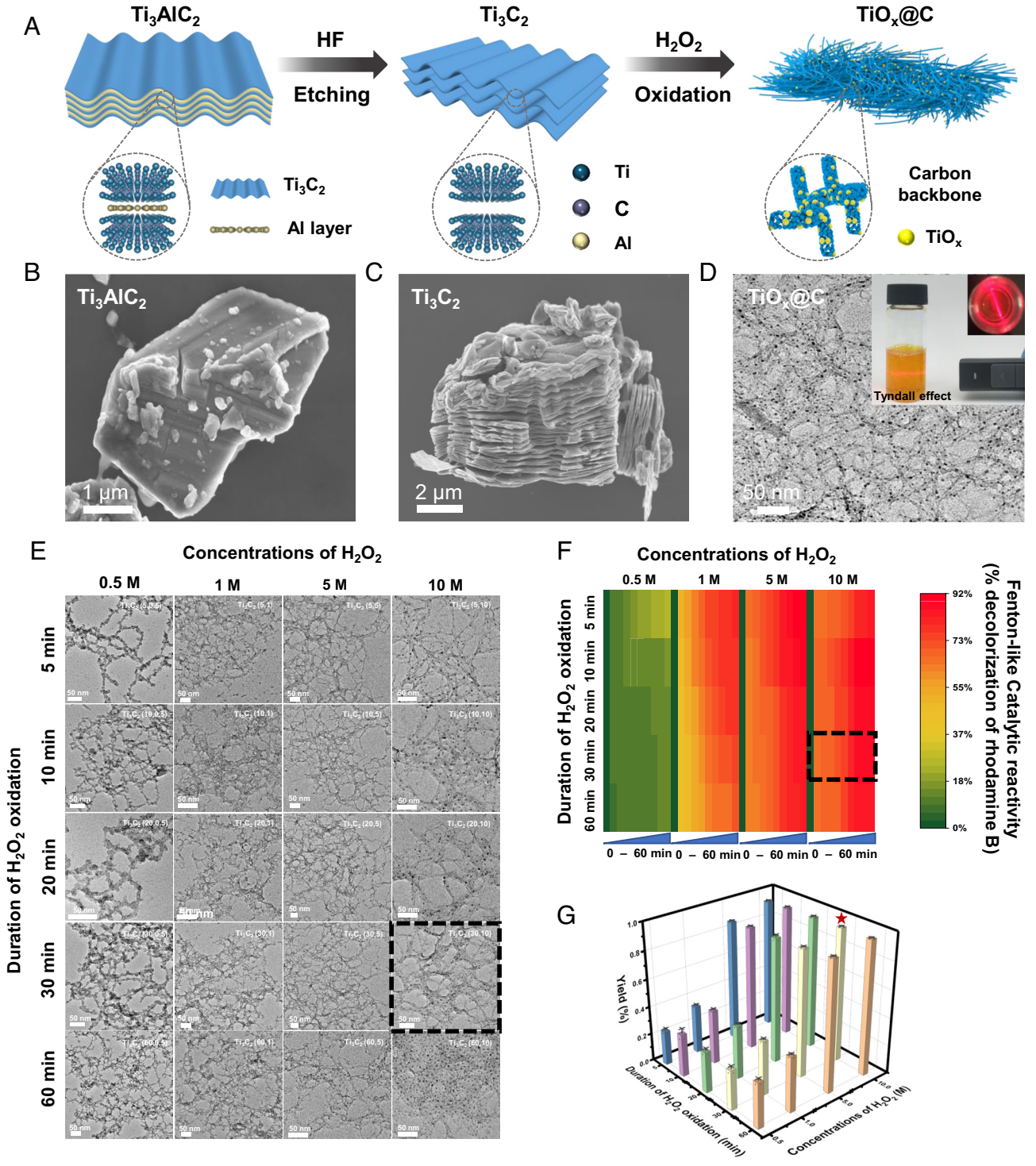

Fig. 1. Synthesis and characterizations of TiO_x@C catalyst. (*A*) Schematic description of in situ formation of TiO_x@C templated by exfoliated Ti_3C_2 MXene. SEM images of bulk Ti_3AlC_2 (*B*) and Ti_3C_2 (*C*) displaying a typical accordion-like structure after HF etching. (*D*) TEM image of TiO_x@C with TiO_x nanoclusters (dark dots) decorated on an amorphous carbon backbone (light gray). *Inset*: photograph of TiO_x@C aqueous dispersion showing the typical Tyndall effect. (*E*) TEM images of TiO_x@C fabricated by increasing concentrations of H_2O_2 (0.5 M, 1 M, 5 M, and 10 M) and duration of oxidation (5 min, 10 min, 20 min, 30 min, and 60 min). (*F*) Heat map of the Fenton-like catalytic performance of TiO_x@C based on decolorization of rhodamine B. Red to green indicates high to low activities. (*G*) Yield (%) of TiO_x@C from oxidation of Ti_3C_2 by variations of H_2O_2 concentrations and duration of oxidation.

signal at g = 1.946 of the exfoliated Ti_3C_2 MXene, suggesting the presence of single Ti vacancy or vacancy clusters after HF etching (*SI Appendix*, Fig. S2). The EPR signal was indicative of the existence of Ti^{3+} defects (28). Based on transmission electron microscopy (TEM) observation, increasing concentrations (0.5 to 10 M) and treatment duration (5 to 60 min) of H_2O_2 improved the uniformity of the nanoclusters decorated on the silk-like structure. And the overall morphology remained the same after the treatment of 10 M H_2O_2 for 30 min, suggesting that the H_2O_2 was fully consumed (Fig. 1*E*). These characteristics suggested a likely composition of the final product, i.e., titanium oxide nanoclusters decorated on thin carbon layers (TiO_x@C). The extent of decolorization of rhodamine B was used to evaluate the Fenton-like catalytic activity of TiO_x@C. As shown in Fig. 1*F*, a higher extent of RhB decolorization was associated with a higher amount of darker dots in the silk-like structure. Moreover, the percent yield of TiO_x@C quantified by the weight percentage of the final product vs. the exfoliated Ti_3C_2 MXene was approximately 97%, showing an almost complete use of the source materials (Fig. 1*G*). Since HF exfoliation of MXene could lead to the breakage of Ti–Al bonds, resulting in Ti vacancy or vacancy clusters on the MXene substrate, it is reasonable to hypothesize that the resulted defects could play a vital role in the formation of TiO_x nanoclusters (23). Since these defects were highly oxophilic, exfoliated MXene was expected to abstract oxygen from chemical compounds such as H_2O_2 to form oxides (29). And such a reaction would allow the in situ formation of nanoclusters with an intimate interface with the MXene substrate (30).

DFT Calculations Revealed the Key Reaction for Nanocluster Formation. DFT calculations were conducted to validate the hypothesis on the in situ formation of TiO_x@C. The free-standing Ti_3C_2 and two typical $Ti_3C_2T_x$ (T_x = –O or –OH) monolayer structural forms were constructed (as shown in Fig. 2*A* and *SI Appendix*, Figs. S3 and S4) with the optimized geometries (types I, II, and III) delineated in details (*SI Appendix*, Figs. S5 and S6). Among them, the type I structure of $Ti_3C_2T_x$ (T_x = –O) unit cells was selected to build up models based on the lowest total energies (Fig. 2*B* and *SI Appendix*, Table S1). The likely adsorption sites for H_2O_2 molecules on the exfoliated MXene were calculated to be twenty-seven adsorption positions (top (T), bridge (B), and hollow (H), nine positions in each case) (*SI Appendix*, Figs. S7 and S8). As shown in Fig. 2*C* and *SI Appendix*, Table S2, the 019 position of hollow (H) was the most likely adsorption site due to the lowest adsorption energy. In contrast to the defect-free MXene (Fig. 2*D*), the presence of surface Ti-deficit vacancies brought distortion to neighboring atoms and led to a clear electronic delocalization (Fig. 2*E*). The H_H atom in the adsorbed H_2O_2 molecule showed a strong interaction with the surface O of Ti-deficit MXene (O_s). The DFT calculations further strengthened our speculation that the surface Ti-deficit vacancies in the exfoliated Ti_3C_2 were the key reactive sites for the formation of TiO_x nanoclusters.

Physicochemical Characterizations and Defect Analyses of TiO_x@C. High-angle annular dark-field microscopy (HAADF–STEM) revealed an average size of 2.66 nm for the TiO_x nanoclusters (Fig. 3*A*) and a uniform distribution of Ti and O in the carbon substrate (Fig. 3*B*). TiO_x@C showed excellent dispersibility with a hydrodynamic diameter of 187.43 ± 11.54 nm and a negative surface charge of –27.57 ± 0.42 mV (*SI Appendix*, Table S3). In the XRD spectra of Ti_3AlC_2 and Ti_3C_2 (Fig. 3*C*), a gradual widening of the 2θ peak at 9.5° indicated increasing interlayer spacing among the exfoliated MXene. The disappearance of the peak after the formation of TiO_x@C suggested that the layered structure no longer existed. And the TiO_x@C did not show any clear indication of crystallinity, which was consistent with the morphology observed under TEM (Figs. 1*F* and 3*D*). This was in clear contrast to loading anatase TiO_2 on exfoliated Ti_3C_2 MXene (*SI Appendix*, Fig. S9), where a clear lattice structure of anatase TiO_2 (a lattice fringe of 0.35 nm) could be obtained. This result indicated that the in situ formation of TiO_x was likely not in the form of typical TiO_2 but as TiO_x nanoclusters embedded in an amorphous structure. Consistently, the selected area electron diffraction (SAED) patterns of TiO_x@C under TEM had no discrete diffraction rings against the clear and continuous crystalline lattice of Ti_3AlC_2 and Ti_3C_2 (*SI Appendix*, Fig. S10). More importantly, lattice distortion defects were prominent throughout the TiO_x@C as revealed by high-resolution TEM (HRTEM) (Fig. 3*E*). The inverse fast Fourier transform (IFFT) profile of two representative areas (I) and (II) showed typical distortion patterns in the TiO_x@C (Fig. 3*F*).

PALS was conducted to determine the types and relative quantities of the defects in TiO_x@C. By detecting the time intervals of positron trapped, the position and types of defects can be distinguished. Meanwhile, the ratio of relative intensities indicated the contents of the respective detects (31, 32). Table 1 summarizes two positron lifetime components (τ_1 and τ_2) that corresponded to two typical defects with relative intensities I_1 and I_2 for TiO_x@C compared with Ti_3AlC_2, Ti_3C_2, and TiO_2@Ti_3C_2. The shorter lifetime τ_1 was ascribed to the defects in the bulk, while the longer lifetime τ_2 was ascribed to the defects on the surface or subsurface of the materials (32, 33). Among them, τ_1 for TiO_x@C (113.0 ps) was the smallest among all samples. This is likely due to the ultrathin structure of TiO_x@C rendering little to no bulk structure. For the surface defects, τ_2 for TiO_x@C (371.0 ps) was close to that of Ti_3C_2 (374.0 ps), indicating that the defects within these materials were likely on the surface or subsurface. More importantly, the ratio of relative intensities (I_2 vs. I_1) provided information on the relative concentrations of the defects within the materials. The I_2 vs. I_1 value of TiO_x@C was the highest (I_2/I_1 = 6.536) among all samples, indicating the highest amount of surface defects. Meanwhile, the I_2 vs. I_1 value of Ti_3C_2 (I_2/I_1 = 1.977) was about 2.5 times higher than that of Ti_3AlC_2 (I_2/I_1 = 0.798), reconfirming that the HF exfoliation process did indeed create surface defects.

A strong EPR signal at g = 2.009 was detected in TiO_x@C (Fig. 4*A*). This signal did not match with the reported EPR signal of Ti^{3+} defects (g = 1.940 to 1.990) (34, 35), O_2–(g = 2.020) (36), or oxygen vacancies (V_o) (g = 2.003) (37), suggesting that the surface Ti vacancy of TiO_x@C was likely situated in a new coordination environment due to the oxidation of H_2O_2. Meanwhile, a relatively weak EPR signal at g = 1.946 was still present (Fig. 4 *A*, *Inset*), indicating that the Ti^{3+} defects previously detected in the exfoliated Ti_3C_2 were still available in the TiO_x@C.

Chemical State and Local Atomic Structure of TiO_x@C. As the evidence of the existence of multivalence-Ti became clearer, XPS was conducted to show the presence of multipeaks of Ti^{2+} (33.31%), Ti^{3+} (45.35%), and Ti^{4+} (21.34%) in the Ti 2p spectrum (Fig. 4*B*). The local structure at the atomic level was further revealed by X-ray absorption near-edge structure (XANES). As shown in Fig. 4*C* and *SI Appendix*, Table S4, the near-edge absorption energy of TiO_x@C was situated among standard samples (i.e. Ti foil, TiO, Ti_2O_3, and TiO_2), indicating the positive charge of $Ti^{\delta+}$ was between Ti^0 and Ti^{4+}. In addition, the first-order derivative of near-edge absorption energy was analyzed to obtain the energy of the white line peak (E_0), which showed a linear relationship with the valence of the Ti element. This allowed the calculation of the titanium element at an

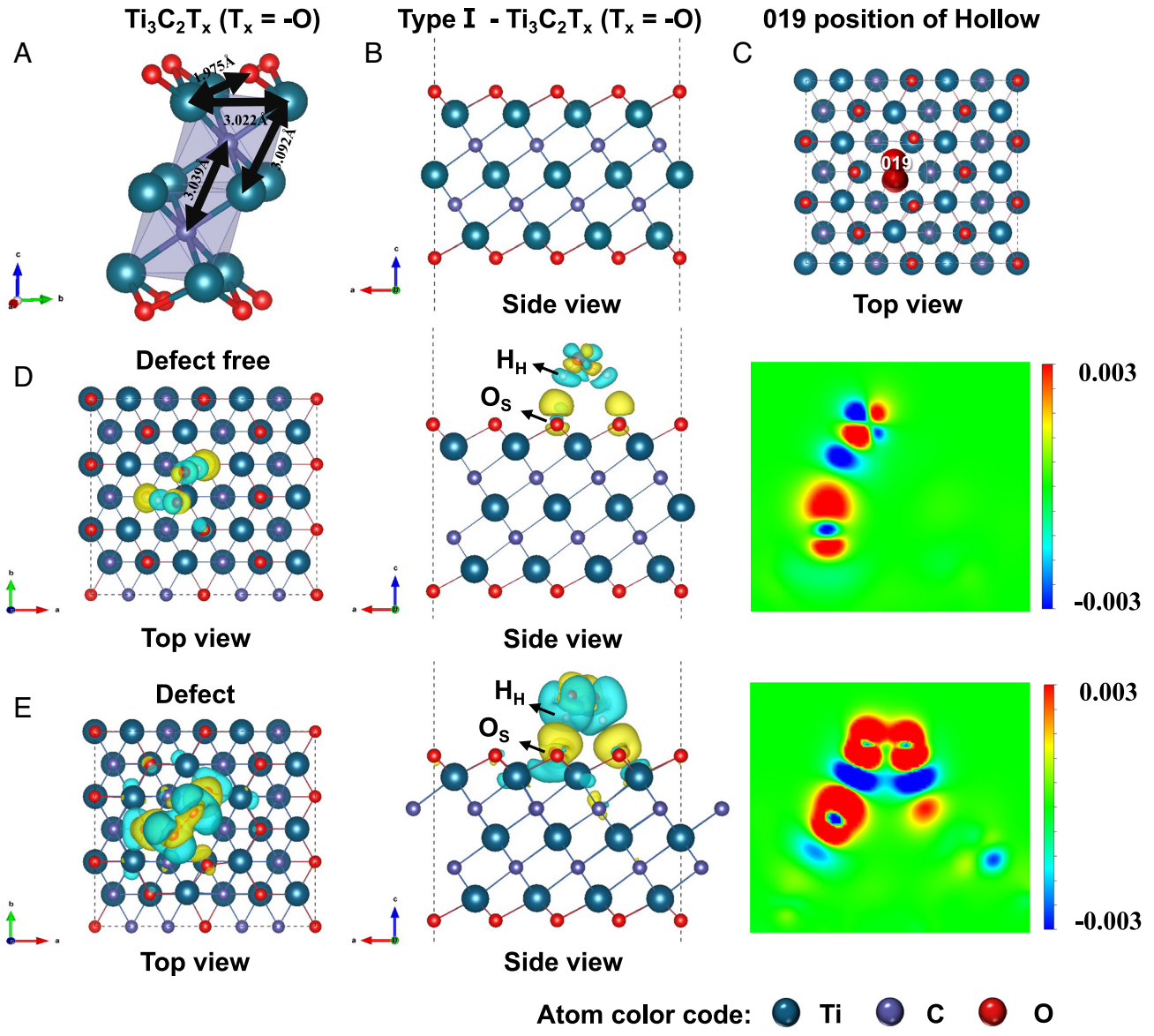

Fig. 2. DFT calculations. (*A*) Optimized geometries of the $Ti_3C_2T_x$ (T_x = −O) monolayer structural forms. (*B*) Side views of type I—$Ti_3C_2T_x$ (T_x = −O). (*C*) Top view of adsorption behaviors between type I—$Ti_3C_2T_x$ (T_x = −O) and H_2O_2 molecule at the lowest energy 019 hollow adsorption site. The bonding charge density of the $Ti_3C_2T_x$ (T_x = −O) at the defect-free system (*D*) and Ti-defected system (*E*). Red and blue colors indicate electron accumulation and depletion, respectively. The color scale is in the units of 0.001 e $bohr^{-3}$. Atom color code: titanium (teal), carbon (indigo blue), and oxygen (red).

average of 2.94^+ oxidation state in TiO_x@C, resulting in x = 1.47 (Fig. 4*D*) (38–40). $TiO_{1.47}$@C was used from here on for the ease of expression. The Ti K-edge XANES analysis (Fig. 4*E*) showed that the edge energy of $TiO_{1.47}$@C was higher than that of Ti_3AlC_2 and Ti_3C_2. And the Ti K-edge extended x-ray absorption fine structure (EXAFS) spectra (*SI Appendix*, Fig. S11) demonstrated that the $k^3\chi(k)$ oscillation displayed a noticeable difference in the range of 2 to 14 $Å^{-1}$ in comparison with pure Ti foil, Ti_3AlC_2, and Ti_3C_2, implying a different local atomic arrangement around Ti. More importantly, the Fourier transform (FT) spectra displayed two peaks in the range of 1.5 to 3.0 Å corresponding to the Ti-O and Ti-C-Ti bonds (Fig. 4*F*). The first-shell (Ti-O) scattering area of $TiO_{1.47}$@C increased significantly against Ti_3AlC_2 and Ti_3C_2, proving the formation of the Ti-O bonds. And the second-shell (Ti-C-Ti) scattering showed a right shift with a remarkable amplitude reduction compared with TiO_2, Ti_3AlC_2, and Ti_3C_2. This was likely a result of collapsed layer structure to form the thin carbon layer (41). The presence of the carbon substrate was important to maintain $TiO_{1.47}$@C at a relative steady state or metastable state. And the thin layer of amorphous carbon was not likely to interfere with the electron transfer during the Fenton-like reaction with H_2O_2 (42, 43).

Fenton-Like Catalytic Performance of $TiO_{1.47}$@C toward the Degradation of Atrazine. The Fenton-like catalytic performance of $TiO_{1.47}$@C was evaluated toward the degradation of the typical agriculture herbicide atrazine (ATZ) via activation of H_2O_2. As shown in Fig. 5*A*, $TiO_{1.47}$@C ([Ti] = 0.1 g L^{-1}) showed superior reactivity to activate H_2O_2 (5 mM) to degrade ATZ (2.5 mg L^{-1}) within 5 min compared with Ti_3AlC_2, Ti_3C_2, and TiO_2@Ti_3C_2 under the same conditions. Neither $TiO_{1.47}$@C nor H_2O_2 (5 mM) alone showed any degradation. The existence of multivalence-$Ti^{\delta+}$ (δ = 0, 2, 3, and 4) was the key to activating H_2O_2 for ATZ degradation.

DMPO-trapped EPR further demonstrated the generation of ·OH and $\cdot O_2-$ in the Fenton-like catalytic reaction. Fig. 5 *B* and *C* showed clear signals from DMPO-·OH and DMPO-$\cdot O_2-$. The introduction of radical scavengers, i.e., p-benzoquinone

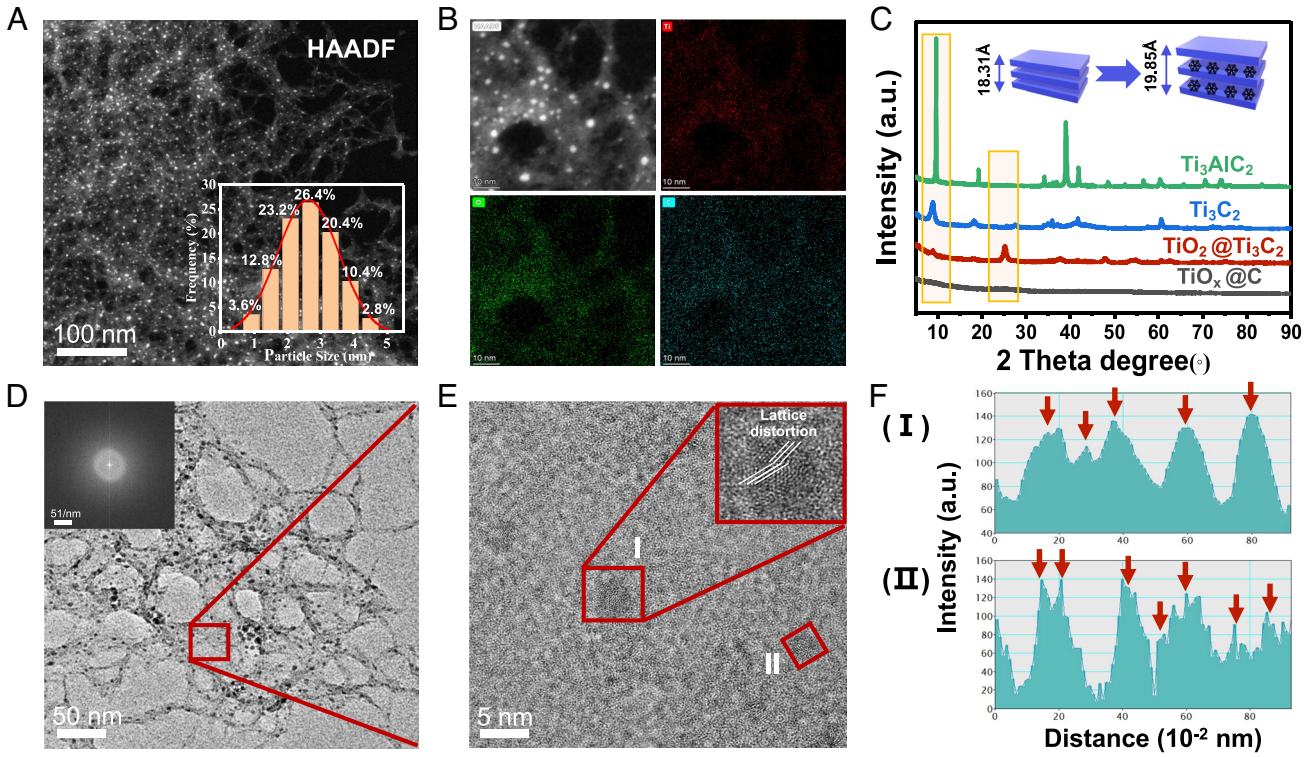

Fig. 3. Structural and defect characterizations of TiO_x@C catalyst. (*A*) HAADF–STEM image of TiO_x@C confirming the presence of TiO_x nanoclusters (bright spots) and the corresponding size distribution (*Inset*). (*B*) Energy-dispersive X-ray elemental mapping of TiO_x@C, suggesting that titanium and oxygen were uniformly distributed in the carbon backbone. (*C*) XRD spectra of Ti_3AlC_2, Ti_3C_2, TiO_2@Ti_3C_2, and TiO_x@C. (*D*) HRTEM image of TiO_x@C and the corresponding electron diffraction pattern image (*Inset*). The red box highlights the area shown in *E*. (*E*) HRTEM image with lattice distortion highlighted (areas I and II). (*F*) Intensity profile of areas I and II in (*E*).

(PBQ), tert-butyl alcohol (TBA), and EDTA-2Na, decreased the extent of ATZ degradation by 3.9%, 29.8%, and 30.3%, respectively. The surface-bound free radical quencher, potassium iodide (KI) was also able to significantly decrease the extent of degradation similar to that of TBA and EDTA-2Na (Fig. 5*D*). These results suggested that the Fenton-like catalytic degradation of ATZ was likely through a surface catalytic process. Consistently, the electrochemically active surface area (ECSA) measurements revealed that $TiO_{1.47}$@C possessed the highest double-layer capacitance (Cdl) value of 6×10^{-5} mF cm^{-2}, suggesting it had more active surface areas for catalytic reactions (Fig. 5*E* and *SI Appendix*, Fig. S12). Moreover, five repeated cycles of Fenton-like reactions showed little changes in the degradation efficiency (Fig. 5*F*). Neither the crystalline phase nor the morphology showed any changes after five Fenton-like reactions (*SI Appendix*, Fig. S13). The shelf life of $TiO_{1.47}$@C was highly desirable as it demonstrated good structural stability beyond 15 mo (*SI Appendix*, Fig. S14). Interestingly, the solution pH (from 3 to 11) had no interference effect on the degradation efficiency (*SI Appendix*, Fig. S15). Such stability was consistent with the surface charge measurement, where the zeta potential of $TiO_{1.47}$@C remained constant within the same pH range (*SI Appendix*, Table S5). This further confirmed that the interactions between the $TiO_{1.47}$@C and H_2O_2 governed the overall catalytic reactivity.

Table 1. Positron lifetime parameters of Ti_3AlC_2, Ti_3C_2, TiO_2@Ti_3C_2, and TiO_x@C

Sample name	τ_1 (ps)	I_1 (%)	τ_2 (ps)	I_2 (%)	I_2/I_1
TiO_x@C	113.0	13.27	371.0	86.73	6.536
Ti_3AlC_2	156.0	55.62	315.0	44.38	0.798
Ti_3C_2	145.0	33.59	374.0	66.41	1.977
TiO_2@Ti_3C_2	158.0	27.01	359.0	72.99	2.702

The transformation products (TPs) of ATZ delineated by UHPLC–QTOF–MS also confirmed the oxidation process. Among the nine typical TPs detected, the formation of deethylatrazine (DEA, m/z 188) and deisopropylatrazine (DIA, m/z 174) was due to deethylation and deisopropylation, respectively (*SI Appendix*, Fig. S16 and Table S6). Similar processes were observed for the transformation from hydroxy atrazine (HA, m/z 198) to deethylhydroxy atrazine (DEHA, m/z 170) and further to deethyldeisopropylhydroxyatrazine (DEIHA, m/z 128). In addition, the oxidation of the amide group in 2-chloro-4-acetamido-6-isopropylamino-1,3,5-triazine (CAIT, m/z 230) might contribute to the formation of partial DEA (m/z 188). The final product DEIHA (m/z 128) was likely formed via successive amide hydrolysis and deisopropylation. The detailed analysis of the seven transformation pathways and three main mechanisms (e.g., dealkylation, alkyl chain oxidation, dechlorination, and hydroxylation) are depicted in Fig. 5*G* and further explained in *SI Appendix*. These results confirmed that the degradation of ATZ was mainly through oxidation, in which the dealkylation was likely initialized by the attack of hydroxyl radical (·OH) and further produced carbon-center radicals that led to a cascade of oxidation events (44). And the main TP CAIT (m/z 230) was formed via the oxidation of an intermediate carbinolamine by hydroxyl radical (·OH) (45). In addition, the excellent degradation efficiencies toward different types of pollutants also indicated that the $TiO_{1.47}$@C/H_2O_2 system was capable of nonselectively decomposing a variety of organic substances in aqueous systems. Compared with the traditional Fenton system, which showed significant generation of Fe sludge after the Fenton reaction, $TiO_{1.47}$@C remained highly dispersed

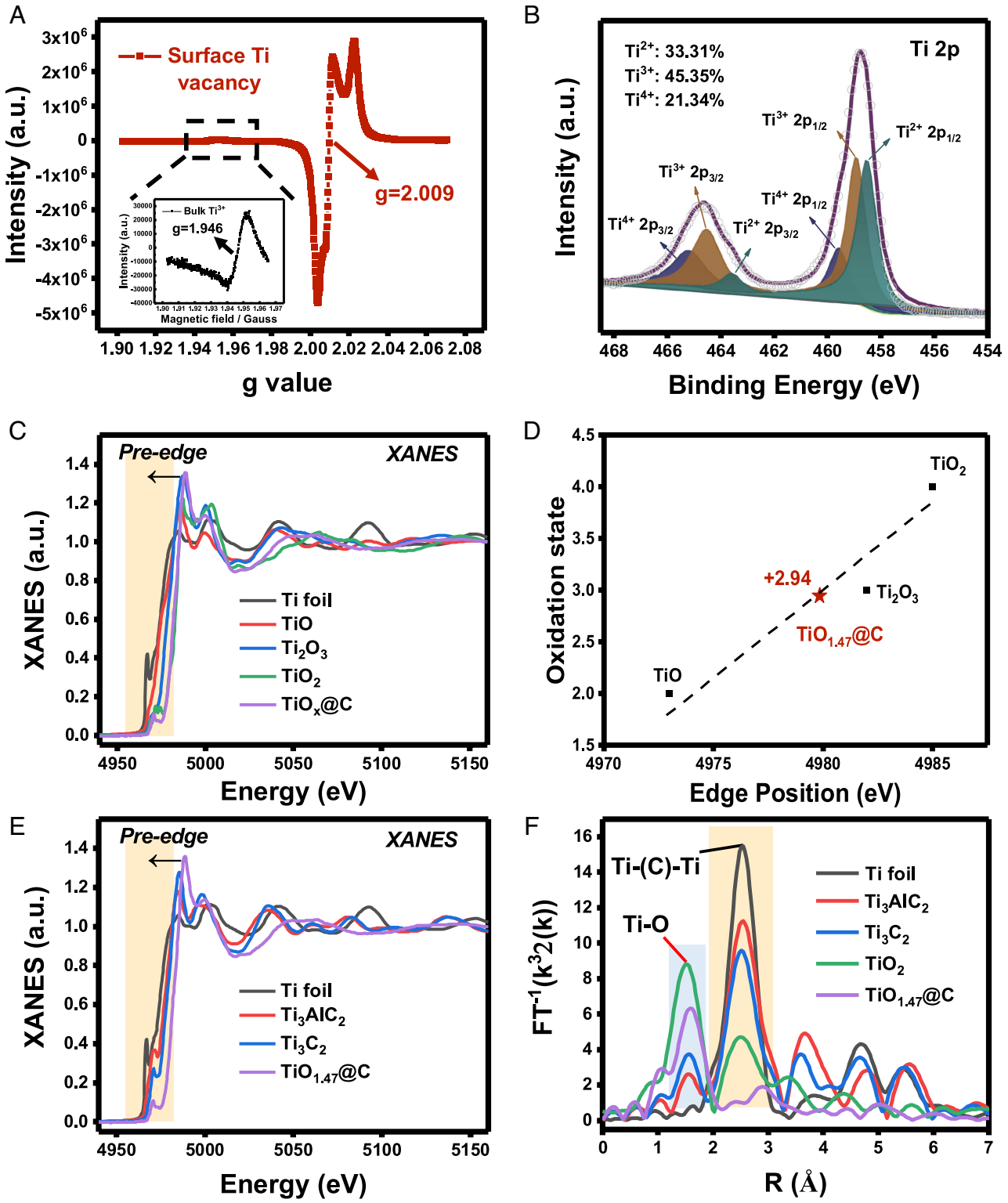

Fig. 4. Chemical state and atomic local structure of TiO_x@C catalyst. (*A*) EPR spectra (77K) of TiO_x@C showing a clear surface Ti vacancy signal (g = 2.009) and a significantly weaker bulk Ti^{3+} signal (g = 1.946, *Inset*). (*B*) High-resolution XPS spectrum of Ti 2p. The percentage of valences of Ti element was calculated as Ti^{2+}: 33.31%, Ti^{3+}: 45.35%, and Ti^{4+}: 21.34%. (*C*) Normalized Ti K-edge XANES spectra of Ti foil, TiO, Ti_2O_3, TiO_2, and TiO_x@C. (*D*) Estimation of the titanium oxidation state in TiO_x@C. According to the XANES spectra of Ti from the edge position of references to TiO, Ti_2O_3, and TiO_2, Ti was calculated to be in an average of 2.94^+ oxidation state in TiO_x@C, with x = 1.47. (*E*) Normalized Ti K-edge XANES spectra of Ti foil, Ti_3AlC_2, Ti_3C_2, and $TiO_{1.47}$@C, respectively. (*F*) The k^3-weighted FT spectra from Ti K-edge EXAFS.

after the degradation (*SI Appendix*, Fig. S17). The excellent dispersibility resulted in some difficulties in recycling and reusing, and embedding these active catalysts onto suitable substrates to form nanocomposites could be a feasible solution (46).

Application of the In Situ Fenton-Like Catalyst Construction Strategy on Other MXene Family Materials. The universal applicability of the in situ strategy was tested on other MXene family materials, e.g., V_2C and Nb_2C. SEM (*SI Appendix*,

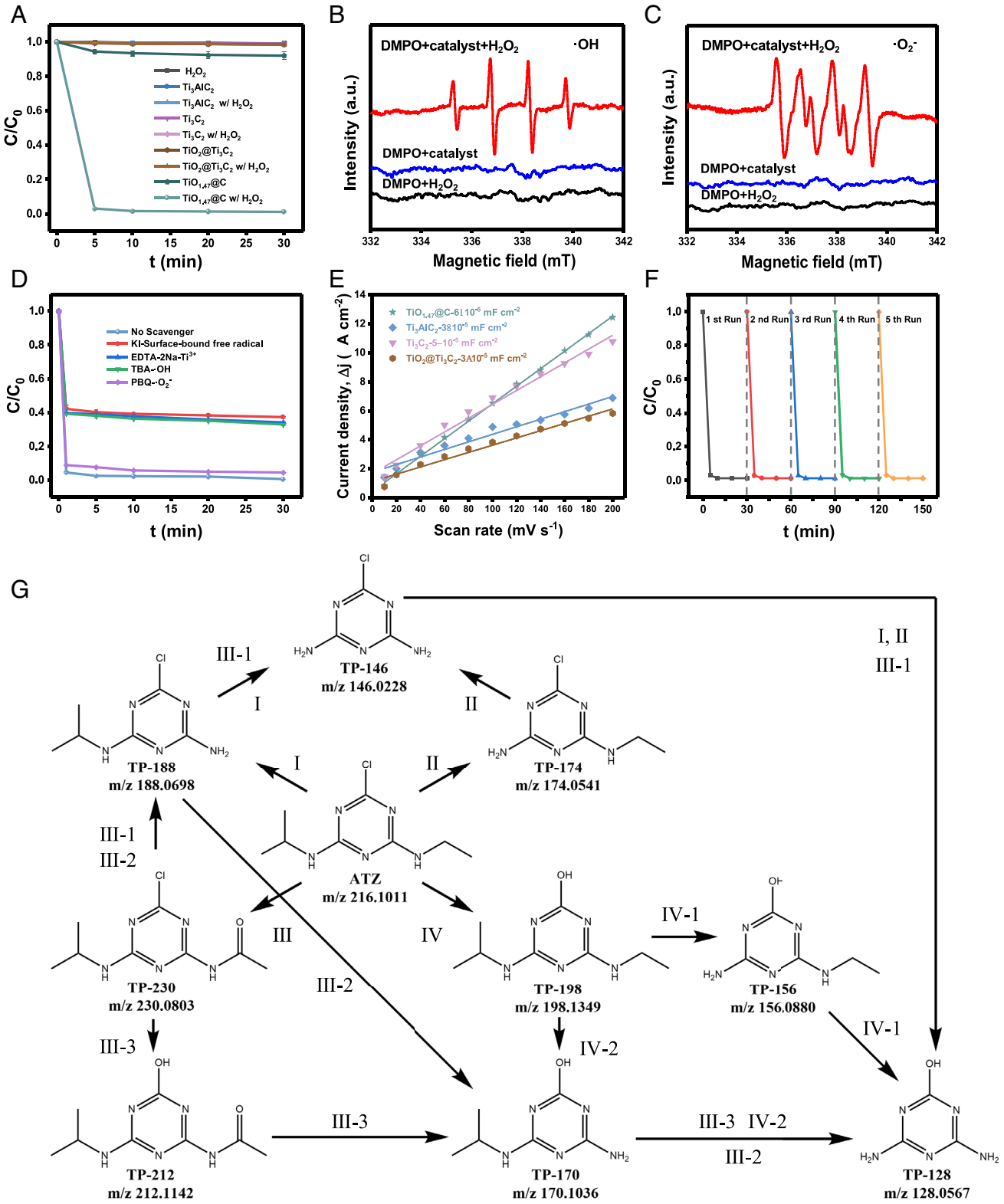

Fig. 5. Fenton-like catalytic performance and stability assessment of $TiO_{1.47}$@C. (*A*) $TiO_{1.47}$@C showed superior Fenton-like catalytic degradation of atrazine. (*B*) DMPO spin-trapping EPR spectra of DMPO-·OH (water system). (*C*) DMPO spin-trapping EPR spectra of DMPO-·O_2– (methanol system). (*D*) Effects of quenching agents (KI, EDTA-2Na, TBA, and PBQ) on the Fenton-like degradation of atrazine. (*E*) Estimated double-layer capacitances of $TiO_{1.47}$@C in comparison with Ti_3AlC_2, Ti_3C_2, and TiO_2@Ti_3C_2. (*F*) Stability assessment of the Fenton-like degradation efficiency for five runs. (*G*) Proposed Fenton-like degradation pathways of atrazine followed by the identification of several intermediates by UHPLC–QTOF–MS. Conditions: [Ti] = 0.1 g L^{-1}, [atrazine] = 2.5 mg L^{-1}, and [H_2O_2] = 5 mM.

Figs. S18 *A* and *B* and S19 *A* and *B*) and TEM (*SI Appendix*, Figs. S18*C* and S19*C*) micrographs showed similar morphological features compared with $TiO_{1.47}$@C. Both materials showed excellent Fenton-like catalytic performance toward the decolorization of RhB (*SI Appendix*, Figs. S18*D* and S19*D*). It is worth noting that the easiness of exfoliation of MXene correlated with the Fenton-like catalytic performance of the resulting catalysts.

In conclusion, by in situ turning defects into catalytic active sites, we have successfully demonstrated a strategy to turn exfoliated MXene into Fenton-like catalysts. The redox reaction between the

Ti-deficit defects after exfoliation and H_2O_2 resulted in highly dispersed $TiO_{1.47}$ nanoclusters decorated on a silk-like carbon substrate. The catalysts showed excellent and stable Fenton-like catalytic activity toward the degradation of RhB and atrazine. Theoretical calculations and defect analyses revealed that the Ti-deficit vacancies were the key to the in situ formation of the $TiO_{1.47}$@C, and the superior Fenton-like catalytic performance came from the abundance of surface defects and the existence of multivalence-$Ti^{\delta+}$ (δ = 0, 2, 3, and 4). Such an approach also applies to other MXene family materials, such as V_2C and Nb_2C. Our work showcased a strategy to use MXene materials as both substrate and multivalent metal precursor for the in situ formation of heterogeneous Fenton-like catalysts.

Materials and Methods

Synthesis of $TiO_{1.47}$@C. Ti_3C_2 MXene was obtained by a common exfoliation method using HF (40%). Dry powder (100 mg) of the exfoliated Ti_3C_2 was then dispersed in deionized water by magnetic stirring at room temperature for 10 min. A mild oxidation reaction was conducted by adding H_2O_2 (0.5 M, 1 M, 5 M, and 10 M) to the Ti_3C_2 suspension, and the reaction was kept at 0°C under an ice water bath for a series of duration (5 min, 10 min, 20 min, 30 min, and 60 min). The resulted dispersion was centrifuged for 20 min at 8,000 rpm to remove large agglomerates, and the supernatant was collected as the final product. All samples obtained were placed under 4°C for storage.

Physicochemical Characterizations. Microscopic and spectroscopic techniques were applied for physicochemical characterizations. The surface morphology and microstructure were characterized by SEM (Hitachi S4800, 3 kV) and TEM (JEM-2011, 200 kV). HRTEM and scanning transmission modes (STEM) were performed using TALOS F200X, 200 kV, equipped with an energy-dispersive spectrometer. The crystalline structure of as-prepared samples was characterized based on X-ray diffraction (XRD) patterns using a D-8 advanced X-ray diffractometer (Bruker-AXS) with Cu Kα radiation operated at a voltage of 40 kV and a current of 40 mA at a scanning speed of 5° min^{-1}. The concentration of Ti element of the as-prepared samples was analyzed by an inductively coupled plasma spectrometer (ICP; ICP7700, Agilent). The hydrodynamic size and zeta potential of the as-prepared samples were measured by a Zetasizer Nano ZS instrument (Malvern Instruments). X-ray photoelectron spectrum (XPS) analysis was conducted with a PHI-1600 X-ray photoelectron spectroscope equipped with Al Kα radiation, and the binding energy was calibrated by the C 1 s peak (284.8 eV). EPR spectroscopy measurements were carried out on a Bruker EMX EPR spectrometer at an X-band frequency of 9.363 GHz, sweep width of 500.00 gauss, and center field of 3390.00 gauss, with 5,5-dimethyl-1-pyrroline N-oxide (DMPO) as the spin-trapping agents for reactive species. The information on various defects was characterized by positron annihilation lifetime spectroscopy (PALS) under an ORTEC-583 fast–fast coincident system using a coincidence spectrometer at room temperature. Further details can be found in *SI Appendix*.

XAFS Measurements and EXAFS Analysis. Chemical speciation of Ti was determined by K-edge XANES. XANES spectra of titanium in $TiO_{1.47}$@C powder were obtained with a Si (111) double crystal monochromator in the transmission model using the beamline of 14W1A in the Shanghai Synchrotron Radiation Facility. Ti foil, TiO, Ti_2O_3, TiO_2, Ti_3AlC_2, and Ti_3C_2 were selected as references. The electron beam energy of the storage ring was 3.5 GeV, and the maximum stored current was approximately 210 mA. The acquired EXAFS data were processed according to the standard procedures using the ATHENA module implemented in IFEFFIT software packages. The k^3-weighted EXAFS spectra were obtained by subtracting the postedge background from the overall absorption and then normalizing with respect to the edge-jump step. Subsequently, k^3-weighted χ(k) data in the k-space ranging from 2 to 14 $Å^{-1}$ were Fourier transformed to real (R) space using a Hanning window (dk = 1.0 $Å^{-1}$) to separate the EXAFS contributions from different coordination shells (47, 48).

DFT Calculations. All calculations were based on the DFT using Vienna ab initio simulation package (VASP). The electron–ion interaction was described by the projected augmented wave (PAW) method. The exchange–correlation functional was described within the generalized gradient approximation (GGA) of the Perdew–Burke–Ernzerhof (PBE) functional. The van der Waals interactions were modeled using the DFT-D3. The Brillouin zone integration was obtained by an 8 × 8 × 1 Monkhorst–Pack k-points mesh, and the energy cutoff was set to 500 eV. The atomic positions were optimized using the conjugate gradient algorithm and the convergence threshold was set at 1×10^{-6} eV $atom^{-1}$. For all the calculations, the Hellmann–Feynman force on each atom was relaxed to a convergence criterion of 0.01 eV $Å^{-1}$.

Data, Materials, and Software Availability. All study data are included in the article and *SI Appendix*.

ACKNOWLEDGMENTS. This work was supported by the National Key Research and Development Program of China (no. 2018YFC1803100), the National Natural Science Foundation of China (no. 21777116), and the Fundamental Research Funds for the Central Universities.

Author affiliations: [a]College of Environmental Science and Engineering, Biomedical Multidisciplinary Innovation Research Institute, Shanghai East Hospital, Tongji University, Shanghai 200092, China; [b]Key Laboratory of Yangtze River Water Environment, Shanghai Institute of Pollution Control and Ecological Security, Tongji University, Shanghai 200092, China; [c]Chinese Academy of Sciences (CAS) Key Laboratory for Biomedical Effects of Nanomaterials and Nanosafety & Chinese Academy of Sciences and The University of Hong Kong (CAS-HKU) Joint Laboratory of Metallomics on Health and Environment, Institute of High Energy Physics, Beijing 100049, China; [d]University of Chinese Academy of Sciences, Beijing 100049, China; [e]Key Laboratory of Nanodevices and Applications, Suzhou Institute of Nano-Tech and Nano-Bionics, Chinese Academy of Sciences, Suzhou 215123, China; [f]Department of Chemistry, Hong Kong Baptist University, Kowloon Tong, Hong Kong Special Administrative Region 000000, China; and [g]State Key Laboratory of Pollution Control and Resource Reuse, College of Environmental Science and Engineering, Tongji University, Shanghai 200092, China

1. M. A. Shannon *et al.*, Science and technology for water purification in the coming decades. *Nature* **452**, 301–310 (2008).
2. J. Wang, S. Li, Q. Qin, C. Peng, Sustainable and feasible reagent-free electro-Fenton via sequential dual-cathode electrocatalysis. *Proc. Natl. Acad. Sci. U.S.A.* **118**, e2108573118 (2021).
3. B. Qiao *et al.*, Single-atom catalysis of CO oxidation using Pt_1/FeO_x. *Nat. Chem.* **3**, 634–641 (2011).
4. X. Zhou *et al.*, Identification of Fenton-like active Cu sites by heteroatom modulation of electronic density. *Proc. Natl. Acad. Sci. U.S.A.* **119**, e2119492119 (2022).
5. Y. Peng, B. Lu, S. Chen, Carbon-supported single atom catalysts for electrochemical energy conversion and storage. *Adv. Mater.* **30**, 1801995 (2018).
6. G. Liu *et al.*, MoS_2 monolayer catalyst doped with isolated Co atoms for the hydrodeoxygenation reaction. *Nat. Chem.* **9**, 810–816 (2017).
7. R. J. White, R. Luque, V. L. Budarin, J. H. Clark, D. J. Macquarrie, Supported metal nanoparticles on porous materials. Methods and applications. *Chem. Soc. Rev.* **38**, 481–494 (2009).
8. J.-X. Wu *et al.*, Graphene-like hydrogen-bonded melamine-cyanuric acid supramolecular nanosheets as pseudo-porous catalyst support. *Adv. Mater.* **33**, 2007368 (2021).
9. Y. Yin *et al.*, Boosting Fenton-like reactions via single atom Fe catalysis. *Environ. Sci. Technol.* **53**, 11391–11400 (2019).
10. Z. Zhang *et al.*, The simplest construction of single-site catalysts by the synergism of micropore trapping and nitrogen anchoring. *Nat. Commun.* **10**, 1657 (2019).
11. M. Dhiman, V. Polshettiwar, Supported single atom and pseudo-single atom of metals as sustainable heterogeneous nanocatalysts. *Chemcatchem* **10**, 881–906 (2018).
12. V. Ramalingam *et al.*, Heteroatom-mediated interactions between ruthenium single atoms and an MXene support for efficient hydrogen evolution. *Adv. Mater.* **31**, 1903841 (2019).
13. X. Li *et al.*, Single cobalt atoms anchored on porous N-doped graphene with dual reaction sites for efficient Fenton-like catalysis. *J. Am. Chem. Soc.* **140**, 12469–12475 (2018).
14. X. Li *et al.*, Single-atom Pt as co-catalyst for enhanced photocatalytic H_2 evolution. *Adv. Mater.* **28**, 2427–2431 (2016).
15. H. Fei *et al.*, General synthesis and definitive structural identification of MN_4C_4 single-atom catalysts with tunable electrocatalytic activities. *Nat. Catal.* **1**, 63–72 (2018).
16. J. Yang *et al.*, Efficient and robust hydrogen evolution: Phosphorus nitride imide nanotubes as supports for anchoring single ruthenium sites. *Angew. Chem. Int. Ed.* **57**, 9495–9500 (2018).
17. Y. Jiang, Y. Qin, T. Yu, S. Lin, Synthesis of sponge-like TiO_2 with surface-phase junctions for enhanced visible-light photocatalytic performance. *Chin. Chem. Lett.* **32**, 1823–1826 (2021).
18. M. Naguib, V. N. Mochalin, M. W. Barsoum, Y. Gogotsi, 25th anniversary article: MXenes: A new family of two-dimensional materials. *Adv. Mater.* **26**, 992–1005 (2014).
19. M. Naguib *et al.*, Two-dimensional nanocrystals produced by exfoliation of Ti_3AlC_2. *Adv. Mater.* **23**, 4248–4253 (2011).
20. M. Naguib, M. W. Barsoum, Y. Gogotsi, Ten years of progress in the synthesis and development of MXenes. *Adv. Mater.* **33**, 2103393 (2021).
21. J. Zhang *et al.*, Single platinum atoms immobilized on an MXene as an efficient catalyst for the hydrogen evolution reaction. *Nat. Catal.* **1**, 985–992 (2018).
22. X. Sang *et al.*, Atomic defects in monolayer titanium carbide ($Ti_3C_2T_x$) MXene. *ACS Nano*. **10**, 9193–9200 (2016).

23. D. Zhao *et al.*, MXene (Ti_3C_2) vacancy-confined single-atom catalyst for efficient functionalization of CO_2. *J. Am. Chem. Soc.* **141**, 4086–4093 (2019).
24. X. Li *et al.*, Nonoxidized MXene quantum dots prepared by microexplosion method for cancer catalytic therapy. *Adv. Funct. Mater.* **30**, 2000308 (2020).
25. M. Zhang, Y. Niu, Y. Xu, Heterogeneous Fenton-like magnetic nanosphere coated with vanadium oxide quantum dots for enhanced organic dyes decolorization. *J. Colloid Interface Sci.* **579**, 269–281 (2020).
26. S. R. Pouran, A. R. A. Aziz, W. M. A. W. Daud, Z. Embong, Niobium substituted magnetite as a strong heterogeneous Fenton catalyst for wastewater treatment. *Appl. Surf. Sci.* **351**, 175–187 (2015).
27. A. D. Bokare, W. Choi, Review of iron-free Fenton-like systems for activating H_2O_2 in advanced oxidation processes. *J. Hazard. Mater.* **275**, 121–135 (2014).
28. Y. Zhou, C. Chen, N. Wang, Y. Li, H. Ding, Stable Ti^{3+} self-doped anatase-rutile mixed TiO_2 with enhanced visible light utilization and durability. *J. Phys. Chem. C* **120**, 6116–6124 (2016).
29. X. Cheng *et al.*, A titanium-based photo-Fenton bifunctional catalyst of mp-MXene/TiO_{2-x} nanodots for dramatic enhancement of catalytic efficiency in advanced oxidation processes. *Chem. Commun.* **54**, 11622–11625 (2018).
30. C. Chen *et al.*, MoS_2-on-MXene heterostructures as highly reversible anode materials for lithium-ion batteries. *Angew. Chem. Int. Ed.* **57**, 1846–1850 (2018).
31. M. Kong *et al.*, Tuning the relative concentration ratio of bulk defects to surface defects in TiO_2 nanocrystals leads to high photocatalytic efficiency. *J. Am. Chem. Soc.* **133**, 16414–16417 (2011).
32. C. Li *et al.*, Enhanced visible-light-driven photocatalytic hydrogen generation using $NiCo_2S_4$/CdS nanocomposites. *Chem. Eng. J.* **378**, 122089 (2019).
33. S. Dutta *et al.*, Annealing effect on nano-ZnO powder studied from positron lifetime and optical absorption spectroscopy. *J. Appl. Phys.* **100**, 114328 (2006).
34. V. M. Khomenko, K. Langer, H. Rager, A. Fett, Electronic absorption by Ti^{3+} ions and electron delocalization in synthetic blue rutile. *Phys. Chem. Miner.* **25**, 338–346 (1998).
35. S. Wang *et al.*, Titanium-defected undoped anatase TiO_2 with p-type conductivity, room-temperature ferromagnetism, and remarkable photocatalytic performance. *J. Am. Chem. Soc.* **137**, 2975–2983 (2015).
36. M. Anpo *et al.*, Generation of superoxide ions at oxide surfaces. *Top. Catal.* **8**, 189–198 (1999).
37. H. Liu *et al.*, The enhancement of TiO_2 photocatalytic activity by hydrogen thermal treatment. *Chemosphere* **50**, 39–46 (2003).
38. H. Zhao *et al.*, The role of Cu_1-O_3 species in single-atom Cu/ZrO_2 catalyst for CO_2 hydrogenation. *Nat. Catal.* **5**, 818–831 (2022).
39. E. Zhang *et al.*, Engineering the local atomic environments of indum single-atom catalysts for efficient electrochemical production of hydrogen peroxide. *Angew. Chem. Int. Ed.* **61**, e202117347 (2022).
40. F. Zhang *et al.*, High-efficiency electrosynthesis of hydrogen peroxide from oxygen reduction enabled by a tungsten single atom catalyst with unique terdentate N_1O_2 coordination. *Adv. Funct. Mater.* **32**, 2110224 (2021).
41. R. Lotfi, M. Naguib, D. E. Yilmaz, J. Nanda, A. C. T. van Duin, A comparative study on the oxidation of two-dimensional Ti_3C_2 MXene structures in different environments. *J. Mater. Chem. A* **6**, 12733–12743 (2018).
42. F. Guinea, Charge distribution and screening in layered graphene systems. *Phys. Rev. B* **75**, 235433 (2007).
43. H. Chen *et al.*, Measurement of interlayer screening length of layered graphene by plasmonic nanostructure resonances. *J. Phys. Chem. C* **117**, 22211–22217 (2013).
44. A. Tauber, C. von Sonntag, Products and kinetics of the OH-radical-induced dealkylation of atrazine. *Acta Hydrochim. Hydrobiol.* **28**, 15–23 (2000).
45. S. Nelieu, L. Kerhoas, J. Einhorn, Degradation of atrazine into ammeline by combined ozone/hydrogen peroxide treatment in water. *Environ. Sci. Technol.* **34**, 430–437 (2000).
46. R. A. Vaia, H. D. Wagner, Framework for nanocomposites. *Mater. Today* **7**, 32–37 (2004).
47. J. Ding *et al.*, Single-particle analysis for structure and iron chemistry of atmospheric particulate matter. *Anal. Chem.* **92**, 975–982 (2020).
48. J. Liu *et al.*, Rapid degradation and high renal clearance of Cu_3BiS_3 nanodots for efficient cancer diagnosis and photothermal therapy in vivo. *ACS Nano*. **10**, 4587–4598 (2016).